

A physics-encoded Fourier neural operator approach for surrogate modeling of divergence-free stress fields in solids

Mohammad S. Khorrami^{1,*}, Pawan Goyal², Jaber R. Mianroodi¹,
Bob Svendsen^{1,3}, Peter Benner², Dierk Raabe¹

¹Microstructure Physics and Alloy Design,
Max-Planck Institute for Sustainable Materials, Düsseldorf, Germany

²Computational Methods in Systems and Control Theory,
Max-Planck Institute for Dynamics of Complex Technical Systems, Magdeburg, Germany

³Material Mechanics, RWTH Aachen University, Aachen, Germany

*Corresponding Author: m.khorrami@mpie.de

Abstract

The purpose of the current work is the development of a so-called physics-encoded Fourier neural operator (PeFNO) for surrogate modeling of the quasi-static equilibrium stress field in solids. Rather than accounting for constraints from physics in the loss function as done in the (now standard) physics-informed approach, the physics-encoded approach incorporates or “encodes” such constraints directly into the network or operator architecture. As a result, in contrast to the physics-informed approach in which only training is physically constrained, both training and output are physically constrained in the physics-encoded approach. For the current constraint of divergence-free stress, a novel encoding approach based on a stress potential is proposed.

As a “proof-of-concept” example application of the proposed PeFNO, a heterogeneous polycrystalline material consisting of isotropic elastic grains subject to uniaxial extension is considered. Stress field data for training are obtained from the numerical solution of a corresponding boundary-value problem for quasi-static mechanical equilibrium. This data is also employed to train an analogous physics-guided FNO (PgFNO) and physics-informed FNO (PiFNO) for comparison. As confirmed by this comparison and as expected on the basis of their differences, the output of the trained PeFNO is significantly more accurate in satisfying mechanical equilibrium than the output of either the trained PgFNO or the trained PiFNO.

Keywords: Scientific machine learning, Fourier neural operators, physics-constrained neural operators, divergence-free stress, mechanical response, polycrystal

1 Introduction

Given the inherent lack and sparsity of data for most physical phenomena as well as their complexity, the development of surrogate numerical models for these phenomena based on (artificial) neural networks (NNs) often includes constraints from physics to improve model robustness. As discussed recently for example by [Faroughi et al. \(2024\)](#), the resulting physics-constrained NNs are currently of three types: (i) physics-guided (PgNNs), (ii) physics-informed (PiNNs), and (iii) physics-encoded (PeNNs). For all three types, the training and testing data are constrained to be physical; PiNNs and PeNNs are based in addition on further physical constraints. In the case of PiNNs, these constraints are incorporated into the loss function (for training/testing), whereas for PeNNs, they are incorporated into (“encoded” in) the network architecture. The basic rational or motivation behind the idea of constrained training and / or output is to reduce the sensitivity of trained NN/NO accuracy to the size of the data set.

By far the most common of these three types are PgNNs and PiNNs. PiNNs in particular have been developed for various problems in science and engineering ([Cuomo et al., 2022](#)), such as computational fluid dynamics ([Cai et al., 2021a](#); [Mahmoudabadbozchelou et al., 2022](#)) or heat transfer ([Cai et al., 2021b](#); [Oommen and Srinivasan, 2022](#); [Xu et al., 2023](#)). Additional examples of PgNNs and PiNNs for computational fluid flow are discussed by [Faroughi et al. \(2024, Tables 2, 4, 5\)](#). Analogously, a number of PgNNs and PiNNs have been developed for surrogate numerical modeling in computational solid mechanics ([Abueidda et al., 2021](#); [Bai et al., 2023](#); [Diao et al., 2023](#); [Goswami et al., 2020](#); [Khorrami et al., 2023](#); [Kumar and Kochmann, 2022](#); [Mianroodi et al., 2021](#); [Wessels et al., 2022](#); [Yang et al., 2023](#)); see also [Faroughi et al. \(2024, Tables 3, 6, 7\)](#).

Among the types of physics-constrained NNs mentioned above, PeNNs are the most challenging to develop (e.g., [Faroughi et al., 2024, §4](#)) and consequently the least common in the literature. Advantages of PeNNs include much less sensitivity to data sparsity than exhibited by PgNNs and PiNNs. Prominent examples of PeNNs include (i) physics-encoded recurrent convolutional neural network (PeRCNN) and (ii) neural ordinary differential equations (NeuralODE). NeuralPDE ([Dulny et al., 2021](#)) represents an extension of NeuralODE to PDEs by combining the method of lines and NeuralODE in a multilayer convolutional NN. Being dependent on the method of lines, NeuralPDE is not directly applicable to certain kinds of PDEs, e.g., elliptical second-order PDEs.

Methodologically more closely related to the current work is that of [Richter-Powell et al. \(2022\)](#), who developed a PeNN for divergence-free vector fields (e.g., the velocity field in the case of incompressible flow) in computational fluid dynamics. In contrast to the current approach suggested here, their very interesting approach

(i) is limited to vector fields, (ii) is based on the Hodge decomposition of differential 1-forms, and (iii) employs function approximation (i.e., NNs) and automatic differentiation.

In computational solid mechanics, PeNNs are rare; for example, [Faroughi et al. \(2024, Table 8\)](#) document no such PeNN. In fact, to our knowledge, the only PeNN for computational solid mechanics in the literature is the so-called constitutive artificial NN (CANN) of [Linka and Kuhl \(2023\)](#) for constitutive modeling of isotropic elastic solids. More specifically, CANN represents a PeNN for finite-deformation isotropic hyperelasticity which exploits tensor invariants and so-called structure tensors (e.g., [Svendsen, 1994](#); [Zheng, 1994](#)) to parameterize the network, and encodes physically relevant mathematical properties such as polyconvexity in the network architecture.

Rather than the function-based approximation of neural networks, so-called neural operators (NOs: e.g., [Faroughi et al., 2024, §5](#)) employ approximation based on functionals. Advantages of NOs over NNs include for example insensitivity to numerical resolution. Examples of NOs include deep operator networks (DeepONets) ([Lu et al., 2019, 2021](#)) and Fourier neural operators (FNOs) ([Kovachki et al., 2023; Li et al., 2021](#)). In particular, PgNOs and PiNOs have been developed for surrogate numerical modeling in computational solid mechanics, including heterogeneous materials ([Kapoor et al., 2022](#)), linear elastic fracture mechanics ([Goswami et al., 2023, 2022](#)), or even production by three-dimensional printing ([Rashid et al., 2022](#)).

The purpose of the current work is the development of a PeFNO for surrogate numerical modeling of quasi-static mechanical equilibrium and the corresponding divergence-free stress field. This is based on generalization of the network/operator architecture and especially its output layer to encode divergence-free stress with the help of a stress potential. In particular, the architecture of the current PeFNO represents a corresponding direct generalization of the FNO from [Li et al. \(2021\)](#). To our knowledge, neither a PeNN, nor a PeNO, of this type for surrogate numerical modeling of the quasi-static equilibrium stress field has appeared in the literature up to this point.

The paper is organized as follows. Section 2 begins with a treatment and discussion of aspects common to the development of physics-constrained NNs and NOs for the quasi-static equilibrium stress field in solids. To facilitate this and comparison with the literature, the term "neural approximation" (NA) is employed for both NNs and NOs in this work (this term was also used for example by [Richter-Powell et al., 2022](#)). Common aspects of NAs include in particular the (i) architecture and (ii) loss function. In this context, the current approach to encode quasi-static mechanical equilibrium (i.e., divergence-free stress) in the NA

architecture via a stress potential is treated in detail. To demonstrate the capabilities of the resulting PeFNO for divergence-free stress, it is applied in Section 3 to surrogate modeling of the stress field in a polycrystalline solid and compared with analogous Pg- and PiFNOs. Synthetic stress field data for training is generated via numerical solution of a physical boundary value problem (BVP) for quasi-static mechanical equilibrium in polycrystals consisting of isotropic elastic grains subject to uniaxial extension. The paper ends in Section 4 with a summary and outlook. To address a broader audience, the treatment and presentation to follow is mostly conceptual and descriptive in character. Because of their scientific importance, as well as for the more technically inclined reader, the mathematical and computational details relevant to the current PeFNO for surrogate modeling of divergence-free stress are summarized in the Supplementary Information.

2 Physics-constrained NAs for the stress field

For brevity, the treatment to follow is restricted to the case of geometric-non-linear solid mechanics (e.g., [Truesdell and Noll, 1965](#); [Šilhavý, 1997](#)). The corresponding treatment for the geometric-linear case is briefly summarized in the Supplementary Information. In the non-linear case, the relevant stress measure is the first Piola-Kirchhoff stress, represented here for simplicity by the matrix of its Cartesian components

$$\mathbf{P} = \begin{bmatrix} P_{11} & P_{12} & P_{13} \\ P_{21} & P_{22} & P_{23} \\ P_{31} & P_{32} & P_{33} \end{bmatrix}. \quad (1)$$

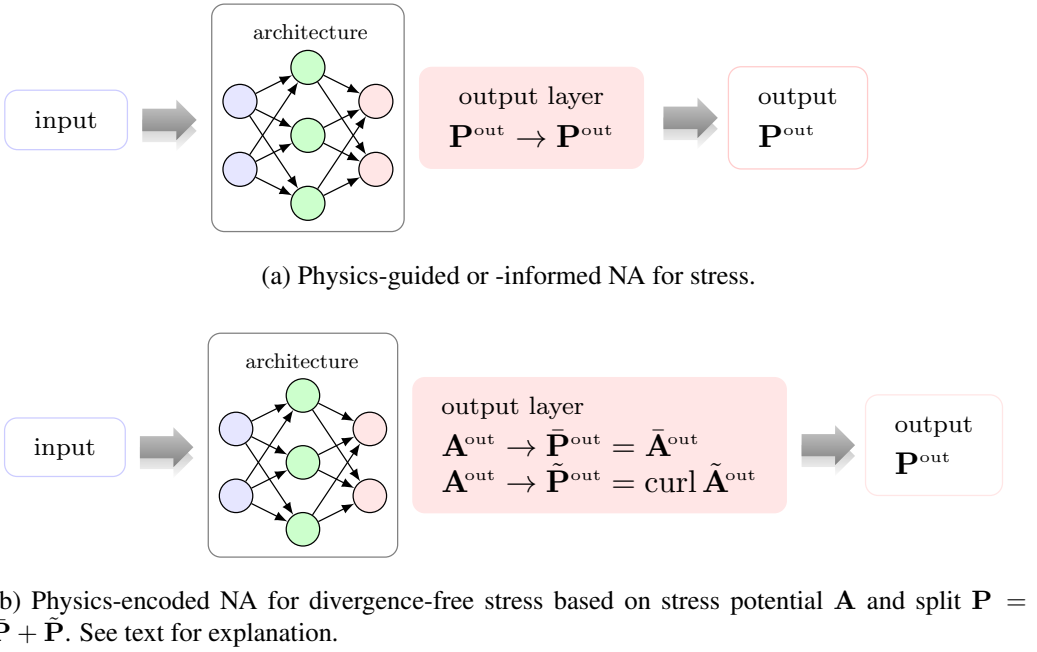
In terms of \mathbf{P} , quasi-static mechanical equilibrium takes the form

$$\operatorname{div} \mathbf{P} = \begin{bmatrix} P_{11,1} + P_{12,2} + P_{13,3} \\ P_{21,1} + P_{22,2} + P_{23,3} \\ P_{31,1} + P_{32,2} + P_{33,3} \end{bmatrix} = \mathbf{0}, \quad (2)$$

with $P_{ij,k} := \partial P_{ij} / \partial x_k$.

As usual, the training of NAs is based on data; in the current case, the relevant data $\mathbf{P}_1^{\text{dat}}, \dots, \mathbf{P}_{n_{\text{dat}}}^{\text{dat}}$ for the quasi-static equilibrium stress field satisfy $\operatorname{div} \mathbf{P}_a^{\text{dat}} = \mathbf{0}$ for $a = 1, \dots, n_{\text{dat}}$. In principle, then, the output \mathbf{P}^{out} of any NA trained with such data should also satisfy $\operatorname{div} \mathbf{P}^{\text{out}} = \mathbf{0}$; in practice of course, $\operatorname{div} \mathbf{P}^{\text{out}} \neq \mathbf{0}$, due for example to issues such as the inherent sparsity of the data. As shown in more detail below, encoding this constraint in the NA architecture is the most robust way to ensure that \mathbf{P}^{out} is divergence-free. In the current work, this encoding is

based on a stress potential \mathbf{A} . A schematic comparison of this with other physics-constrained NAs for the stress field is given in Figure 1.



(b) Physics-encoded NA for divergence-free stress based on stress potential \mathbf{A} and split $\mathbf{P} = \bar{\mathbf{P}} + \tilde{\mathbf{P}}$. See text for explanation.

Figure 1. Schematics of physics-constrained NAs. In all cases, input (e.g., material properties, boundary conditions, or the deformation history) is transferred by the input layer (violet) to the hidden layers (green; only one is shown for simplicity). These in turn transform the input into \mathbf{P}^{out} via an output layer (light red). See text for more details and discussion.

The hidden layers (green in Figure 1) in NNs are based for example on a convolutional architecture such as U-Net (e.g., [Khorrami et al., 2023](#); [Mianroodi et al., 2021](#)) or other "deep" architectures (e.g., [Faroughi et al., 2024](#)). In the FNO, these layers are parameterized by linear weights and biases as well as by the kernel of a linear integral operator (e.g., [Li et al., 2021](#)). As depicted in Figure 1(b), the output layer (light red) in the physics-encoded case projects the potential field \mathbf{A}^{out} from the hidden layers onto its mean value $\bar{\mathbf{A}}^{\text{out}}$ and its fluctuation part $\tilde{\mathbf{A}}^{\text{out}} = \mathbf{A}^{\text{out}} - \bar{\mathbf{A}}^{\text{out}}$ on the region of interest (see the Supplementary Information). These in turn are transformed by the output layer into $\bar{\mathbf{P}}^{\text{out}}$ and $\tilde{\mathbf{P}}^{\text{out}}$, respectively, such that $\text{div } \mathbf{P}^{\text{out}} = \text{div } \tilde{\mathbf{P}}^{\text{out}} = \text{div curl } \tilde{\mathbf{A}}^{\text{out}} = \mathbf{0}$. In PeNNs, such operator relations are evaluated in discretized form for example via automatic differentiation given a differentiable architecture (e.g., [Richter-Powell et al., 2022](#)). In the PeFNO developed in the current work, these are evaluated with the help of Fourier methods and the corresponding discretized algebraic relations in Fourier

space as documented in the Supplementary Information.

3 Example application

As a computational example of the current PeFNO for divergence-free stress, consider its application to the surrogate modeling of the stress field in a heterogeneous solid with a grain microstructure. For comparison, analogous Pg- and PiFNOs are also considered. Since the main purpose of the paper is the development of methods for material modeling, the computational example is based for simplicity on a number of simplifying assumptions. These include (i) isotropic elastic grains, (ii) limitation of FNO optimization to training, and related to this (iii) use of fixed values for FNO hyperparameters. Some of these simplifications are discussed in more detail below.

3.1 Synthetic stress field data for training

Stress field data for FNO training are obtained from the numerical solution of a BVP for quasi-static mechanical equilibrium on a periodic unit cell U containing the grain microstructure. To this end, the stress in each grain is modeled here by the isotropic elastic Saint Venant-Kirchhoff relation

$$\mathbf{P} = \lambda (\mathbf{I} \cdot \mathbf{E}) \mathbf{F} + 2\mu \mathbf{F} \mathbf{E} \quad (3)$$

depending on the Lamé elastic moduli λ and μ . In this relation, \mathbf{F} and

$$\mathbf{E} = \frac{1}{2}(\mathbf{F}^T \mathbf{F} - \mathbf{I}) \quad (4)$$

represent the matrices of Cartesian components of the deformation gradient and the symmetric Green strain, respectively, analogous to Equation (1) for \mathbf{P} . In addition, $\mathbf{I} \cdot \mathbf{E} = E_{11} + E_{22} + E_{33}$ is the trace of \mathbf{E} .

Each microstructure in the data set represents a random distribution of grain morphologies and grain material property value distributions for Young's modulus $E \in [50, 300]$ GPa and Poisson's ratio $\nu \in [0.2, 0.4]$ determining $\lambda = E\nu/((1 + \nu)(1 - 2\nu))$ and $\mu = E/(2(1 + \nu))$ in Equation (3). An example of such a microstructure is shown in Figure 2.

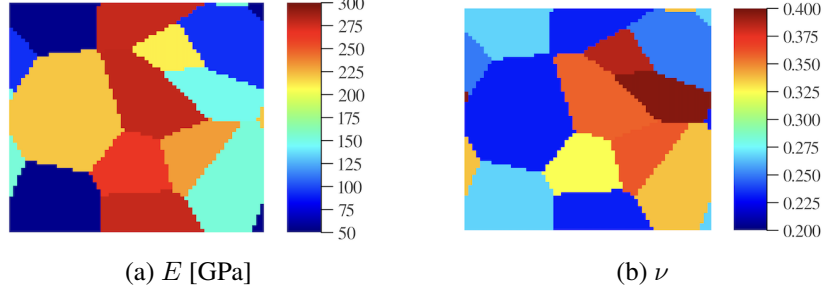


Figure 2. Example microstructure in 2D unit cell U (x_1 horizontal, x_2 vertical).

The stress data set is generated for a set of n_{dat} such microstructures, all subject to the same prescribed mean local deformation $\bar{\mathbf{F}}$. The corresponding BVP based in particular on Equations (2)-(3) has been implemented and numerically solved using spectral methods (Khorrami et al., 2020; Willot, 2015) and the software toolkit DAMASK (Roters et al., 2019).

3.2 FNO training

Training of the PgFNO and PeFNO is based on the weighted mean absolute error

$$L_{\text{dat}} := \frac{1}{n_{\text{dat}}} \sum_{a=1}^{n_{\text{dat}}} \sum_{b=1}^{n_{\text{dis}}} |\mathbf{W}_{ab}^{\text{dat}} \cdot (\mathbf{P}_{ab}^{\text{out}} - \mathbf{P}_{ab}^{\text{dat}})| \quad (5)$$

for the loss function, where n_{dis} is the number of discretization points. In this relation, \mathbf{P}_{ab} is the stress field value at the discretization point position $\mathbf{x}_b = (x_1, x_2, x_3)_b$ ($b = 1, \dots, n_{\text{dis}}$) in the a^{th} microstructure ($a = 1, \dots, n_{\text{dat}}$) of the data set, and $\mathbf{W}_{ab}^{\text{dat}}$ the corresponding weighting matrix. Training is based on $n_{\text{dat}} = 1000$ in the sequel.

For the current example based on the grain microstructure in Figure 2, values for the components of $\mathbf{W}_{ab}^{\text{dat}}$ are determined as follows. Given a uniform numerical discretization of U , the number of data in regions of uniform stress (i.e., grain interiors) is much larger than the number of data in regions of non-uniform stress (i.e., grain boundaries). Consequently, unweighted training automatically results in trained FNO stress field output which underestimates spatial variations in the stress field, especially near grain boundaries. To compensate for this bias, $\mathbf{W}_{ab}^{\text{dat}}$ components are proportional to the sum of 1 and a term determined by the magnitude of the gradient of the corresponding component of $\mathbf{P}_a^{\text{dat}}$ at \mathbf{x}_b normalized by this component (examples of the components of $\mathbf{W}_{ab}^{\text{dat}}$ are shown in Figure 4 below).

For the PiFNO, the loss function takes the form

$$L := L_{\text{dat}} + c L_{\text{div}}, \quad L_{\text{div}} := \frac{1}{n_{\text{dat}}} \sum_{a=1}^{n_{\text{dat}}} \sum_{b=1}^{n_{\text{dis}}} |(\text{div } \mathbf{P}_a^{\text{out}})_b|, \quad (6)$$

where c is a scalar hyperparameter. In contrast to L_{dat} , note that L_{div} is unweighted. Like the operator relations in the output layer of the PeFNO based on Figure 1(b), $(\text{div } \mathbf{P}_a^{\text{out}})_b$ and L_{div} are evaluated with the help of Fourier methods and the corresponding algebraic relations in Fourier space (given in the Supplementary Information).

3.3 FNO architecture and hyperparameters

Following in essence [Li et al. \(2021\)](#), the architecture of all FNOs in what follows consists of 1 input layer (violet in Figure 1), 4 hidden layers (light green in Figure 1), and 1 output layer (light red in Figure 1). Each hidden layers contains 20 neurons or "channels" (only three are shown in Figure 1 for simplicity).

The number of neurons per hidden layer, or the number of hidden layers in the architecture, represent so-called hyperparameters. In principle, their values should be optimized during testing and validation of the trained FNO. For simplicity, however, we follow [Li et al. \(2021\)](#) in working with a fixed value for this. They established this value empirically, and showed that increasing this number beyond 20 led to no significant increase in robustness of the trained FNO. Likewise for simplicity, the value of the scalar hyperparameter c in Equation (6) is also fixed here. Unless otherwise specified, $c = 10^{-1}$ in the sequel.

3.4 Results for the stress field

Restricting attention for simplicity to plane deformation of a square unit cell U of side-length l in the x_1 (horizontal), x_2 (vertical) plane, note that $F_{33} = 1$ is constant and $F_{13}, F_{23}, F_{31}, F_{32}$ are identically zero. Then $P_{13} = P_{23} = 0$ and $P_{31} = P_{32} = 0$ hold identically via Equation (3). In the context of plane deformation, the unit cell containing the microstructure is subject to the mean deformation gradient $\bar{F}_{11} = 1, \bar{F}_{22} = 1.004, \bar{F}_{33} = 1$ (all other $\bar{F}_{ij} = 0$) corresponding to uniaxial extension in the x_2 direction and a mean Green strain of $\bar{E}_{22} = 0.401\%$ (all other $\bar{E}_{ij} = 0$). The data and trained FNO results presented in the following are based on the material property distribution shown in Figure 2 (not a part of the training data set) and a uniform discretization of U based on a square lattice or 2D grid with numerical resolution of $n_{\text{dis}} = 64$ in each dimension. The corresponding stress field data are shown in Figure 3.

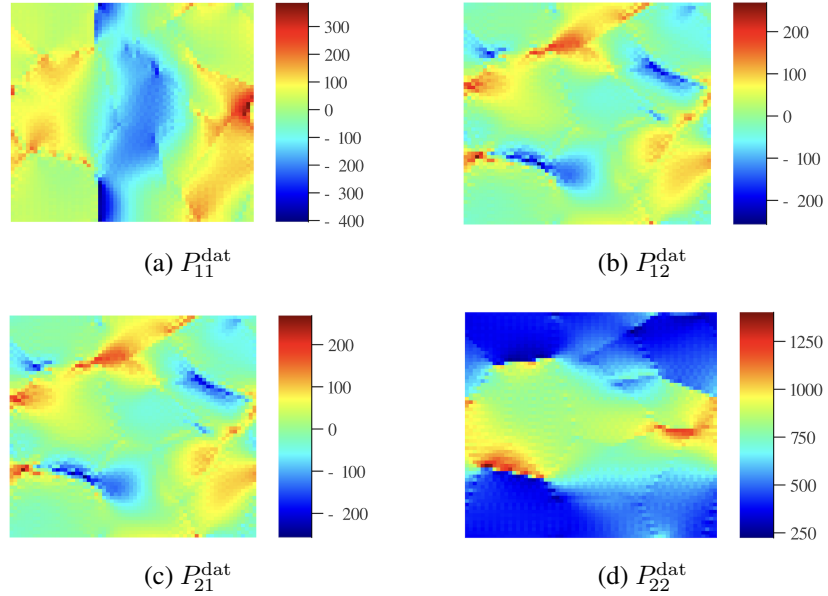


Figure 3. Stress field data in U for uniaxial extension of the microstructure in Figure 2 in the x_2 direction. All values in MPa. Note the differences in scale.

Since P_{12}^{dat} is quite similar to P_{21}^{dat} (due in particular to isotropy), attention is focused for simplicity on P_{11} , P_{21} , and P_{22} in what follows.

Selected components of \mathbf{W}^{dat} for the data in Figure 3 are shown in Figure 4.

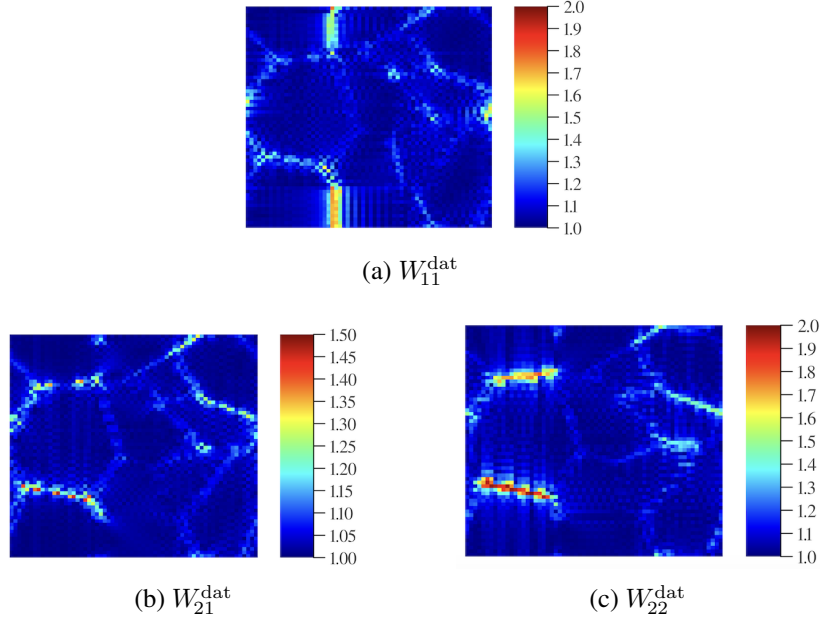


Figure 4. Example components of \mathbf{W}^{dat} [1/l] for data in Figure 3.

Since the components of \mathbf{W}^{dat} are determined by the magnitude of the gradient of the corresponding component of $\mathbf{P}_a^{\text{dat}}$, the results in Figure 4 show that the stress field gradients are largest at grain boundaries. This is also implied by direct inspection of Figure 3. More specifically, this is the case at the grain boundaries with the largest material property contrast (in particular in E), as shown by comparison with the contrast in the material properties at grain boundaries in Figure 2.

Given that $\bar{\mathbf{F}}$ is the same for all data, note that the material property distribution determined by Figure 2 and the numerical discretization is the only input to the trained FNOs in what follows. Results for the largest stress component P_{22} are shown in Figure 5.

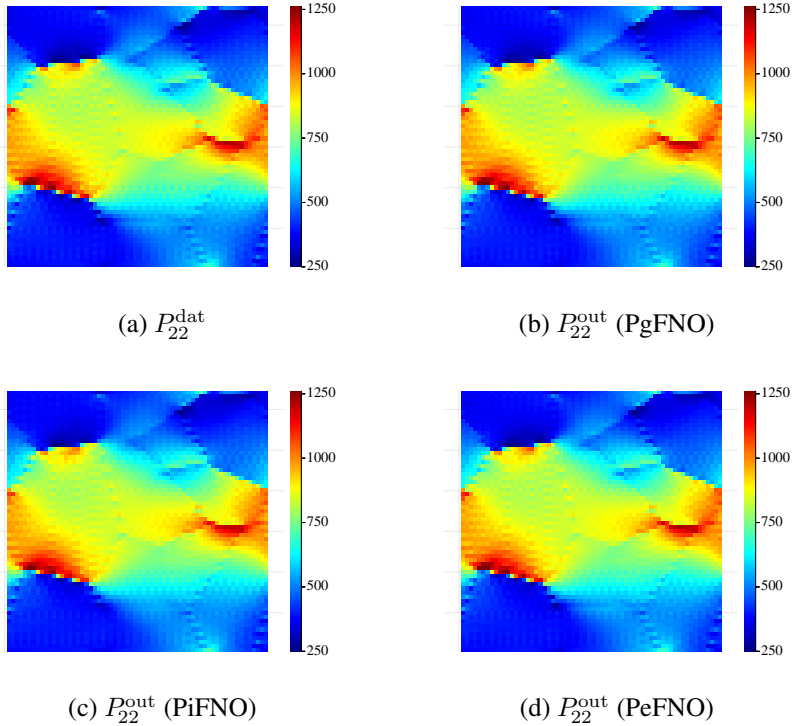


Figure 5. Comparison of P_{22}^{dat} and trained FNO results for P_{22}^{out} in U . All values in MPa.

The magnitude $|P_{22}^{\text{out}} - P_{22}^{\text{dat}}|$ of the error in P_{22}^{out} is displayed in Figure 6.

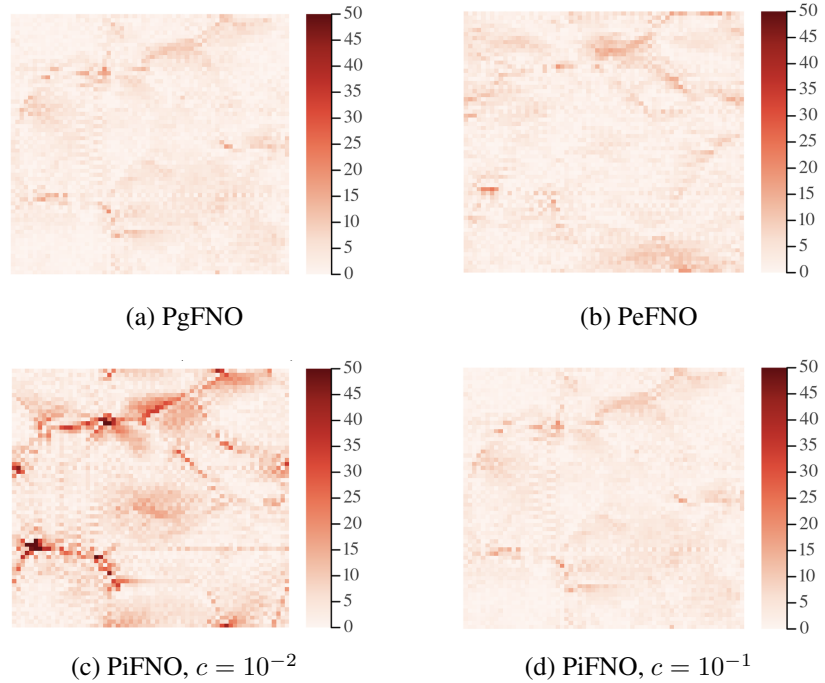


Figure 6. Magnitude $|P_{22}^{\text{out}} - P_{22}^{\text{dat}}|$ of the error in P_{22}^{out} . All values in MPa.

Analogous error results for P_{21}^{out} and P_{11}^{out} are displayed in Figures 7-8.

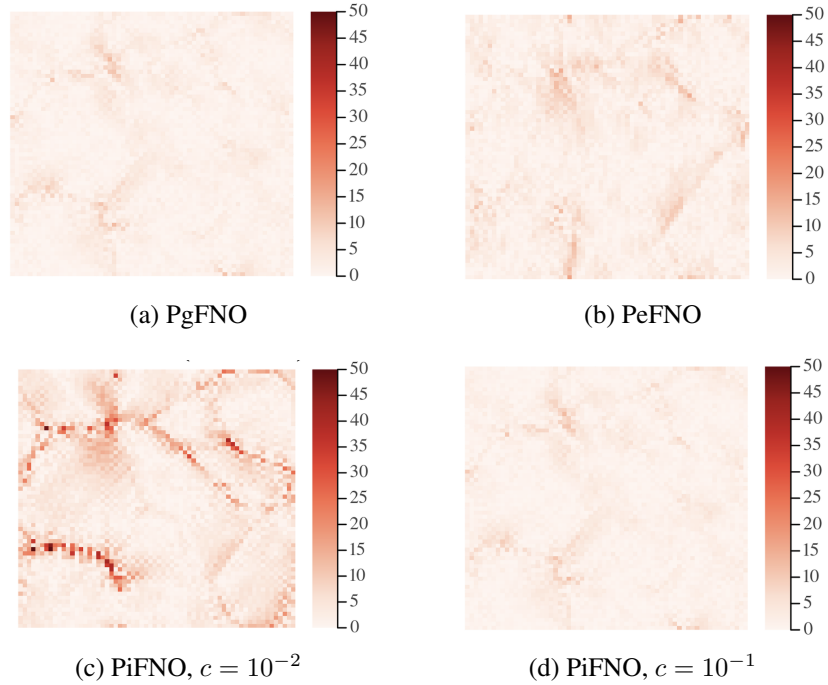


Figure 7. Magnitude $|P_{21}^{\text{out}} - P_{21}^{\text{dat}}|$ of the error in P_{21}^{out} . All values in MPa.

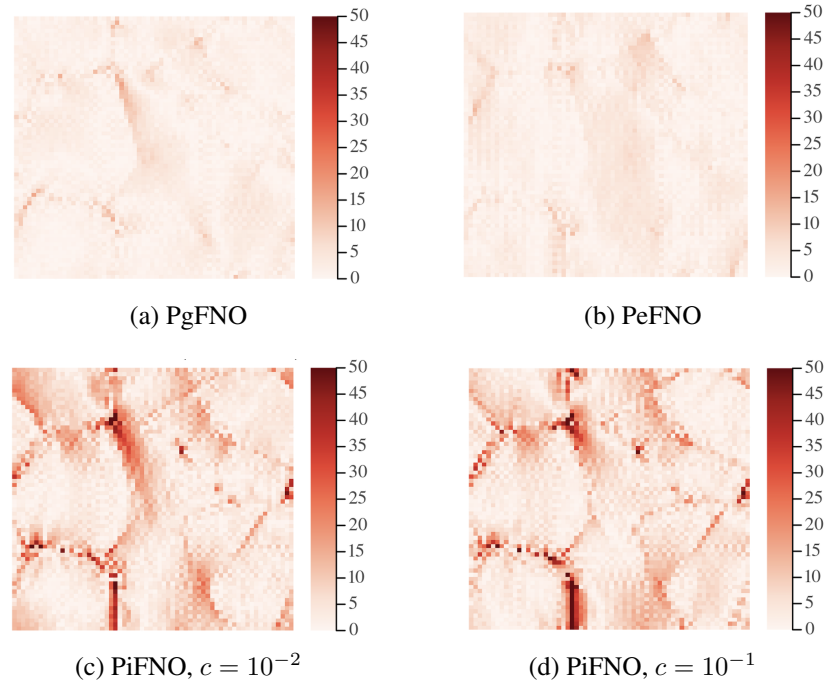


Figure 8. Magnitude $|P_{11}^{\text{out}} - P_{11}^{\text{dat}}|$ of the error in P_{11}^{out} . All values in MPa.

As evident in Figures 6-8, P_{11}^{out} , P_{21}^{out} , and P_{22}^{out} calculated by the trained PiFNO exhibit the largest error of about 50 MPa for $c = 10^{-2}$. Comparison with the material property distribution in Figure 2 implies that the magnitude of this error is correlated with the magnitude of the contrast in material properties across the corresponding grain boundary. Except for the error in P_{11}^{out} , increasing the value of c to 10^{-1} results in a decrease of this error. Recall that training of both the PgFNO and PeFNO based on Equation (5) is independent of L_{div} . Consequently, the larger error in the output of the trained PiFNO is clearly related to the inclusion of L_{div} in the loss function. Also, note that the weighting in Equation (5) appears to be more effective at reducing error in the output of the trained PgFNO and PeFNO than in the trained PiFNO. A possible improvement here could be to include such weighting in L_{div} as well.

3.5 Results for the stress field divergence

To display these results, we work with the form

$$\text{div } \mathbf{p}_r = \text{div } \tilde{\mathbf{p}}_r = \tilde{P}_{r1,1} + \tilde{P}_{r2,2} + \tilde{P}_{r3,3} = 0, \quad r = 1, 2, 3, \quad (7)$$

of quasi-static mechanical equilibrium Equation (2), where $\mathbf{p}_r := (P_{r1}, P_{r2}, P_{r3})$ is the r^{th} row of \mathbf{P} from Equation (1). Since for the current example of plane deformation in (x_1, x_2) , $\text{div } \tilde{\mathbf{p}}_3 = 0$ is identically zero, attention is focused on $\text{div } \tilde{\mathbf{p}}_1^{\text{out}}$ and $\text{div } \tilde{\mathbf{p}}_2^{\text{out}}$ here. Corresponding results are given in Figures 9 and 10.

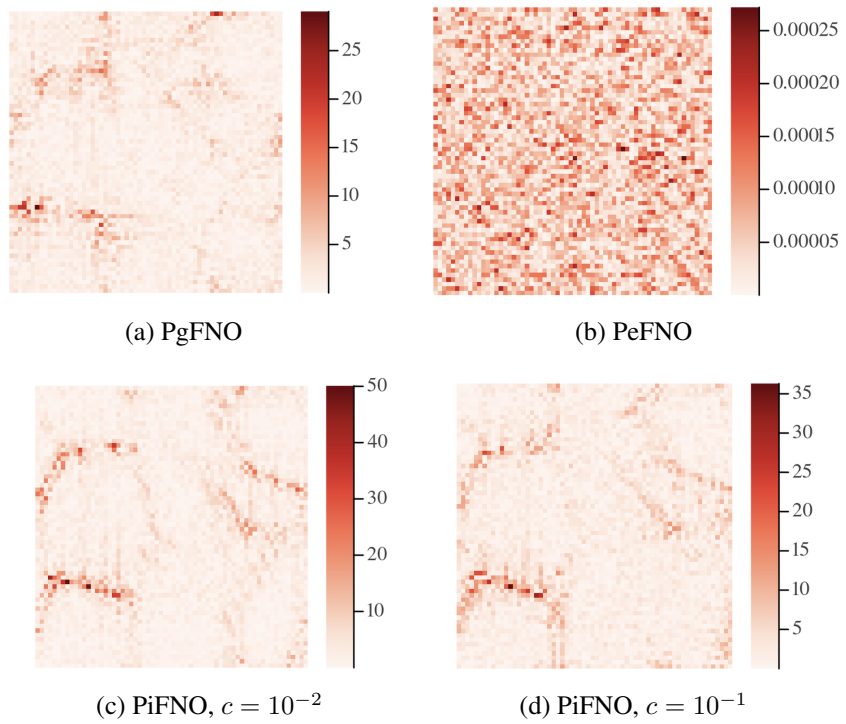


Figure 9. Trained FNO results for $\text{div } \tilde{\mathbf{p}}_1^{\text{out}}$ [MPa/l]. Note the differences in scale.

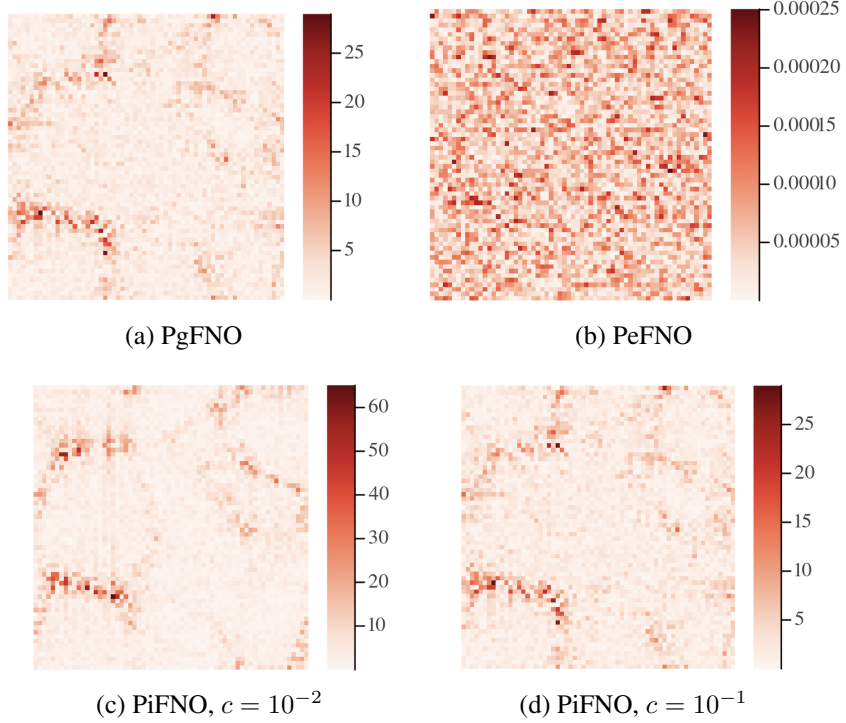


Figure 10. Trained FNO results for $\text{div } \tilde{\mathbf{p}}_2^{\text{out}}$ [MPa/l]. Note the differences in scale.

As expected, the values of $\text{div } \tilde{\mathbf{p}}_1^{\text{out}}$ and $\text{div } \tilde{\mathbf{p}}_2^{\text{out}}$ calculated by the trained PeFNO are significantly smaller than those calculated by the other FNOs. This is also the case for (the magnitude of) $\text{div } \mathbf{P}^{\text{out}}$ since $|\text{div } \mathbf{P}^{\text{out}}| = \sum_{r=1}^3 |\text{div } \tilde{\mathbf{p}}_r^{\text{out}}|$. Note also that the magnitude of the errors in $\text{div } \tilde{\mathbf{p}}_1^{\text{out}}$ and $\text{div } \tilde{\mathbf{p}}_2^{\text{out}}$ calculated by the trained PgFNO and PiFNO are similar and largest at the grain boundaries with the largest contrast in material properties (cf. Figures 2 and 4). One possibility to reduce such error would be to increase the field resolution (i.e., n_{dis}), especially near grain boundaries and more generally in regions of large contrasts in material properties. Another could be to train the FNOs with data on the stress field and its gradient field, at the cost of course of increased effort.

4 Summary and outlook

A physics-encoded Fourier neural operator (PeFNO) has been developed in the current work for the surrogate modeling of quasi-static equilibrium stress field in solids. For the corresponding constraint of divergence-free stress, a novel encoding approach based on a stress potential is proposed. As shown in the current work, inclusion ("encoding") of this constraint in the operator architecture rather

than in the loss function as done in the physics-informed case yields more accurate and robust FNO output for the equilibrium stress field. This is also related to the fact that only the training of the PiFNO is constrained by mechanical equilibrium; in contrast, it constrains both the training and output of the PeFNO.

The neural operators considered in the current work can be improved and refined in a number of ways. One possibility here is inclusion of the deformation gradient \mathbf{F} in the training and operator input data. Another concerns the architecture of the PeFNO for divergence-free stress based on the stress potential \mathbf{A} . Since $\tilde{\mathbf{P}} = \text{curl } \tilde{\mathbf{A}}$ is not invertible, calculating $\tilde{\mathbf{A}}$ as the "anti-curl" of $\tilde{\mathbf{P}}$ is non-unique and a further source of error in operator training. To avoid this, further constraints on $\tilde{\mathbf{A}}$ are necessary. The most common of these is the Coulomb gauge condition $\text{div } \tilde{\mathbf{A}} = \mathbf{0}$. In this case, $\tilde{\mathbf{P}} = \text{curl } \tilde{\mathbf{A}}$ is invertible, and $\bar{\mathbf{P}} = \bar{\mathbf{A}}$ need not be learned, but rather holds identically. A corresponding improved PeFNO architecture is then obtained by adding an additional input layer based on the Coulomb gauge condition. These and other possible further development of the PeFNOs for surrogate computational modeling in solid mechanical represent work in progress to be reported on in the future.

5 References

Abraham, R., Marsden, J.E., Ratiu, T., 1988. Manifolds, Tensor Analysis and Applications. volume 75 of *Applied Mathematical Sciences*. Springer.

Abueidda, D.W., Lu, Q., Koric, S., 2021. Meshless physics-informed deep learning method for three-dimensional solid mechanics. *International Journal for Numerical Methods in Engineering* 122, 7182–7201.

Bai, J., Rabczuk, T., Gupta, A., Alzubaidi, L., Gu, Y., 2023. A physics-informed neural network technique based on a modified loss function for computational 2D and 3D solid mechanics. *Computational Mechanics* 71, 543–562.

Bhatia, H., Norgard, G., Bremer, P.T., 2013. The Helmholtz-Hodge decomposition – a survey. *IEEE Transactions on Visualization and Computer Graphics* 19, 1386–1404.

Cai, S., Mao, Z., Wang, Z., Yin, M., Karniadakis, G.E., 2021a. Physics-informed neural networks (PINNs) for fluid mechanics: A review. *Acta Mechanica Sinica* 37, 1727–1738.

Cai, S., Wang, Z., Wang, S., Perdikaris, P., Karniadakis, G.E., 2021b. Physics-informed neural networks for heat transfer problems. *Journal of Heat Transfer* 143, 060801.

Chadwick, P., 1999. Continuum Mechanics: Concise Theory and Problems. 2nd ed., Dover.

Cuomo, S., Di Cola, V.S., Giampaolo, F., Rozza, G., Raissi, M., Piccialli, F., 2022. Scientific machine learning through physics-informed neural networks: Where we are and what's next. *Journal of Scientific Computing* 92, 88.

Diao, Y., Yang, J., Zhang, Y., Zhang, D., Du, Y., 2023. Solving multi-material problems in solid mechanics using physics-informed neural networks based on domain decomposition technology. *Computer Methods in Applied Mechanics and Engineering* 413, 116120.

Dulny, A., Hotho, A., Krause, A., 2021. NeuralPDE: modelling dynamical systems from data, in: German Conference on Artificial Intelligence, *Kunstliche Intelligenz*, Springer International Publishing. pp. 75–89.

Faroughi, S.A., Pawar, N.M., Fernandes, C., Raissi, M., Das, S., Kalantari, N.K., Kourosh Mahjour, S., 2024. Physics-guided, physics-informed, and physics-encoded neural networks and operators in scientific computing: fluid and solid mechanics. *Journal of Computing and Information Science in Engineering* 24, 040802. doi:[10.1115/1.4064449](https://doi.org/10.1115/1.4064449).

Goswami, S., Anitescu, C., Chakraborty, S., Rabczuk, T., 2020. Transfer learning enhanced physics informed neural network for phase-field modeling of fracture. *Theoretical and Applied Fracture Mechanics* 106, 102447.

Goswami, S., Bora, A., Yu, Y., Karniadakis, G.E., 2023. Physics-informed deep neural operator networks, in: *Machine Learning in Modeling and Simulation: Methods and Applications*. Springer, pp. 219–254.

Goswami, S., Yin, M., Yu, Y., Karniadakis, G.E., 2022. A physics-informed variational DeepONet for predicting crack path in quasi-brittle materials. *Computer Methods in Applied Mechanics and Engineering* 391, 114587.

Kapoor, S., Mianroodi, J.R., Khorrami, M., Siboni, N.S., Svendsen, B., 2022. Comparison of two artificial neural networks trained for the surrogate modeling of stress in materially heterogeneous elastoplastic solids. *arXiv preprint arXiv:2210.16994* .

Khorrami, M., Mianroodi, J.R., Shanthraj, P., Svendsen, B., 2020. Development and comparison of spectral algorithms for numerical modeling of the quasi-static mechanical behavior of inhomogeneous materials. *arXiv preprint arXiv:2009.03762* .

Khorrami, M.S., Mianroodi, J.R., Siboni, N.H., Goyal, P., Svendsen, B., Benner, P., Raabe, D., 2023. An artificial neural network for surrogate modeling of stress fields in viscoplastic polycrystalline materials. *npj Computational Mate-*

rials 9, 37.

Kovachki, N., Li, Z., Liu, B., Azizzadenesheli, K., Bhattacharya, K., Stuart, A., Anandkumar, A., 2023. Neural operators: learning maps between function spaces with application to PDEs. *Journal of Machine Learning Research* 24, 1–97.

Kumar, S., Kochmann, D.M., 2022. What machine learning can do for computational solid mechanics, in: *Current trends and open problems in computational mechanics*. Springer, pp. 275–285.

Li, Z., Kovachki, N., Azizzadenesheli, K., Liu, B., Bhattacharya, K., Stuart, A., Anandkumar, A., 2021. Fourier neural operator for parametric partial differential equations. *arXiv preprint arXiv:2010.08895v3* .

Linka, K., Kuhl, E., 2023. A new family of constitutive artificial neural networks towards automated model discovery. *Computer Methods in Applied Mechanics and Engineering* 403, 115731.

Lu, L., Jin, P., Karniadakis, G.E., 2019. DeepONet: learning nonlinear operators for identifying differential equations based on the universal approximation theorem of operators. *arXiv preprint arXiv:1910.03193*.

Lu, L., Pengzhan, J., Pang, G., Zhang, Z., Karniadakis, G.E., 2021. Learning nonlinear operators via DeepONet based on the universal approximation theorem of operators. *Natural and Machine Intelligence* 3, 218–229.

Mahmoudabadbozchelou, M., Karniadakis, G.E., Jamali, S., 2022. nn-PINNs: non-newtonian physics-informed neural networks for complex fluid modeling. *Soft Matter* 18, 172–185.

Mianroodi, J.R., H. Siboni, N., Raabe, D., 2021. Teaching solid mechanics to artificial intelligence – a fast solver for heterogeneous materials. *Npj Computational Materials* 7, 99.

Oommen, V., Srinivasan, B., 2022. Solving inverse heat transfer problems without surrogate models: a fast, data-sparse, physics-informed neural network approach. *Journal of Computing and Information Science in Engineering* 22, 041012.

Rashid, M.M., Pittie, T., Chakraborty, S., Krishnan, N.A., 2022. Learning the stress-strain fields in digital composites using a Fourier neural operator. *Iscience* 25.

Richter-Powell, J., Lipman, Y., Chen, R.T.Q., 2022. Neural conservation laws: a divergence-free perspective. *arXiv preprint 2210.01741v3*, 1–21.

Roters, F., Diehl, M., Shanthraj, P., Eisenlohr, P., Reuber, C., Wong, S.L., Maiti,

T., Ebrahimi, A., Hochrainer, T., Fabritius, H.O., et al., 2019. DAMASK—The Düsseldorf Advanced Material Simulation Kit for modeling multi-physics crystal plasticity, thermal, and damage phenomena from the single crystal up to the component scale. *Computational Materials Science* 158, 420–478.

Sadd, M.H., 2009. *Elasticity: Theory, Applications, and Numerics*. 2nd ed., Elsevier.

Sorensen, H., Jones, D., Heideman, M., Burrus, C., 1987. Real-valued fast Fourier transform algorithms. *IEEE Transactions on Acoustics, Speech, and Signal Processing* 35, 849–863. doi:[10.1109/TASSP.1987.1165220](https://doi.org/10.1109/TASSP.1987.1165220).

Svendsen, B., 1994. On the representation of constitutive relations using structure tensors. *International Journal of Engineering Science* 32, 1889–1892.

Teodosiu, C., 1982. *Elastic Models of Crystal Defects*. Springer.

Truesdell, C., Noll, W., 1965. The Non-Linear Field Theories of Mechanics. volume III/3 of *Handbuch der Physik*. Springer.

Šilhavý, M., 1997. *The Mechanics and Thermodynamics of Continuous Media*. Springer.

Wessels, H., Böhm, C., Aldakheel, F., Hürgen, M., Haist, M., Lohaus, L., Wriggers, P., 2022. Computational homogenization using convolutional neural networks, in: *Current Trends and Open Problems in Computational Mechanics*. Springer, pp. 569–579.

Willot, F., 2015. Fourier-based schemes for computing the mechanical response of composites with accurate local fields. *Comptes Rendus Mécanique* 343, 232–245.

Xu, J., Wei, H., Bao, H., 2023. Physics-informed neural networks for studying heat transfer in porous media. *International Journal of Heat and Mass Transfer* 217, 124671.

Yang, C., Zhang, Z., Gu, G.X., 2023. Machine learning for solid mechanics, in: *Intelligent Nanotechnology*. Elsevier, pp. 33–45.

Zheng, Q., 1994. Theory of representations for tensor functions – a unified invariant approach to constitutive equations. *Applied Mechanics Reviews* 47(11), 545–587.

Supplementary Information

A physics-encoded Fourier neural operator approach for surrogate modeling of divergence-free stress fields in solids

Mohammad S. Khorrami^{1,*}, Pawan Goyal², Jaber R. Mianroodi¹,
Bob Svendsen^{1,3}, Peter Benner², Dierk Raabe¹

¹Microstructure Physics and Alloy Design,
Max-Planck Institute for Sustainable Materials, Düsseldorf, Germany

²Computational Methods in Systems and Control Theory,
Max-Planck Institute for Dynamics of Complex Technical Systems, Magdeburg, Germany

³Material Mechanics, RWTH Aachen University, Aachen, Germany

*Corresponding Author: m.khorrami@mpie.de

SI.1 Introduction

The purpose of the Supplementary Information is to briefly summarize and document the mathematical background and details relevant to the current work, and in particular to the encoding of divergence-free stress fields in a FNO-based architecture.

As discussed in the paper, encoding in the current approach is based in particular on a stress potential. The mathematical basis for such potentials is the Helmholtz decomposition of vector fields (e.g., [Bhatia et al., 2013](#)). This is briefly summarized in Section [SI.2](#) and compared with the related Hodge decomposition of 1-form fields employed by [Richter-Powell et al. \(2022\)](#) to encode divergence-free vector fields in NN architectures. Central to the current work is a generalization of the Helmholtz decomposition for vector fields to second-order tensor fields also treated in Section [SI.2](#).

Application of the Helmholtz decomposition to stress measures and quasi-static mechanical equilibrium is documented in Section [SI.3](#). For solids, the former include the non-linear first Piola-Kirchhoff (PK) stress in the paper as well as the linear symmetric stress. Fourier series forms of the corresponding potential relations and other relations relevant to the development of the PeFNO are also given in Section [SI.3](#).

The Supplementary Information ends in Section [SI.4](#) with a summary of the computational forms of the relations from Section [SI.3](#) which have been implemented

in the current PeFNO. Included here in particular is a brief technical discussion of the discrete Fourier transform (DFT) for real-valued fields (RDFT). This latter represents the basis of the real-valued fast Fourier transform (RFFT: e.g., [Sorensen et al., 1987](#)) employed in the FNO (e.g., [Li et al., 2021](#)).

The mathematical treatment in the sequel employs the following notation. Three-dimensional Euclidean points or vectors are symbolized by lower case bold italic or greek letters \mathbf{a}, \dots, ζ , and second-order Euclidean tensors by upper case bold italic or greek letters $\mathbf{A}, \dots, \mathbf{Z}$. In particular, let $\mathbf{i}_1, \mathbf{i}_2, \mathbf{i}_3$ represent the Cartesian basis vectors, and \mathbf{I} the identity. The notation $\mathbf{a} \cdot \mathbf{b}$ and $\mathbf{A} \cdot \mathbf{B}$ denotes scalar products. The transpose \mathbf{A}^T of \mathbf{A} is defined by $\mathbf{c} \cdot \mathbf{A}^T \mathbf{b} := \mathbf{b} \cdot \mathbf{A} \mathbf{c}$. The tensor product $\mathbf{a} \otimes \mathbf{b}$ is defined by $(\mathbf{a} \otimes \mathbf{b}) \mathbf{c} := (\mathbf{b} \cdot \mathbf{c}) \mathbf{a}$, and $(\text{axt } \mathbf{a}) \mathbf{b} := \mathbf{a} \times \mathbf{b}$ defines the axial tensor $\text{axt } \mathbf{a}$ of any vector \mathbf{a} . Additional concepts and notation are introduced as needed.

SI.2 Helmholtz & Hodge decompositions

For simplicity, attention is restricted here to fields on unbounded domains.

SI.2.1 Helmholtz decomposition of vector fields

Let ∇ represent the Euclidean gradient operator, and $\nabla \mathbf{u}$ the gradient of a differentiable vector field \mathbf{u} . Likewise, let $\text{div } \mathbf{u}$ represent the divergence, and $\text{curl } \mathbf{u}$ the curl, of \mathbf{u} defined by¹

$$\text{div } \mathbf{u} := \mathbf{I} \cdot \nabla \mathbf{u}, \quad \mathbf{c} \cdot \text{curl } \mathbf{u} := \text{div } \mathbf{u} \times \mathbf{c} = \text{div} (\text{axt } \mathbf{u}) \mathbf{c}, \quad (\text{SI.1})$$

(e.g., [Chadwick, 1999](#), Chapter 1) for constant \mathbf{c} . Given these, the Helmholtz decomposition of \mathbf{u} takes the form

$$\mathbf{u} = \nabla \varsigma + \text{curl } \varphi \quad (\text{SI.2})$$

(e.g., [Bhatia et al., 2013](#)) determined by scalar ς and vector φ potentials. Properties of this split and the potentials include

- ς and φ are determined only up to constants,
- $\varphi + \nabla f$ is also a vector potential for any smooth scalar field f ,
- \mathbf{u} is divergence-free for ς harmonic, i.e., $\text{div } \nabla \varsigma = 0$.

¹Unless restricted by parentheses, all operators apply to everything on their right.

In particular, the trivial scalar potential

$$\varsigma = \text{const.} \quad (\text{SI.3})$$

determines the corresponding special case

$$\mathbf{u} = \text{curl } \varphi \quad (\text{SI.4})$$

of (SI.2) relevant to the encoding of divergence-free vector fields in NN and NO architectures.

SI.2.2 Hodge decomposition of 1-form fields

To encode divergence-free vector fields into NN architectures, Richter-Powell et al. (2022) work with the Hodge decomposition of 1-form fields (e.g., Abraham et al., 1988) rather than with (SI.2). Although they consider the n -dimensional case, for comparison with the current approach, attention is restricted here for simplicity to the physically relevant case $n = 3$.

Let g represent the standard Euclidean metric with $g(\mathbf{a}, \mathbf{b}) = \mathbf{a} \cdot \mathbf{b}$, and ω the standard Euclidean triple product with $\omega(\mathbf{a}, \mathbf{b}, \mathbf{c}) = g(\mathbf{a} \times \mathbf{b}, \mathbf{c})$. The interior product operator ι_a (e.g., Abraham et al., 1988, §5.1) maps g to the 1-covector $\iota_a g$ defined by $(\iota_a g)(\mathbf{b}) := g(\mathbf{a}, \mathbf{b})$, and ω to the 2-covector $\iota_a \omega$ defined by $(\iota_a \omega)(\mathbf{b}, \mathbf{c}) := \omega(\mathbf{a}, \mathbf{b}, \mathbf{c})$. The Hodge star operator \star (e.g., Abraham et al., 1988, Definition 6.2.12) maps k -covectors ($k = 0, \dots, 3$) to $3 - k$ covectors and $\star\star = (-1)^{k(3-k)}$. In particular, note that $\star 1 = \omega$, $\star \omega = 1$, $\star \iota_c g = \iota_c \omega$ and $\star \iota_c \omega = \iota_c g$. In terms of these operations, the Hodge decomposition of the 1-form field $\iota_u g$ dual to \mathbf{u} takes the form

$$\iota_u g = d\varsigma + \star d\iota_\varphi g = \iota_{\nabla \varsigma} g + \iota_{\text{curl } \varphi} g, \quad (\text{SI.5})$$

where ς and φ are the same potentials as in (SI.2), and d is the exterior derivative operator (e.g., Abraham et al., 1988, Chapter 6). To be precise, Richter-Powell et al. (2022) work with the axial tensor $\text{axt } \varphi$ of φ (their \mathbf{A}) as well as the alternative vector potential \mathbf{b} with $\star d \star \iota_b \omega = \iota_\varphi g$. Choice of the trivial scalar potential (SI.3) reduces (SI.5) to

$$\iota_u g = \star d\iota_\varphi g \quad (\text{SI.6})$$

which is identically divergence-free since then $\text{div } \mathbf{u} = \star d\iota_u \omega = \star dd\iota_\varphi g = 0$.

For vector fields \mathbf{u} and their 1-form duals $\iota_u g$, the Helmholtz (SI.2) and Hodge (SI.5) decompositions are clearly equivalent. In contrast to the Helmholtz case, however, the Hodge decomposition is not readily generalizable to higher- and in particular second-order tensor fields like the stress.

SI.2.3 Helmholtz decomposition for tensor fields

This is obtained from the vector form (SI.2) as follows. Any differentiable second-order tensor field \mathbf{S} and constant vector \mathbf{c} induce a corresponding vector field $\mathbf{v} = \mathbf{S}^T \mathbf{c}$ whose divergence and curl are defined by (SI.1). Using these, one can define the corresponding operators

$$\mathbf{c} \cdot \operatorname{div} \mathbf{S} := \operatorname{div} \mathbf{S}^T \mathbf{c}, \quad (\operatorname{curl} \mathbf{S})^T \mathbf{c} := \operatorname{curl} \mathbf{S}^T \mathbf{c}, \quad (\text{SI.7})$$

on \mathbf{S} . Analogously, substitution of $\mathbf{u} = \mathbf{S}^T \mathbf{c}$, $\varsigma = \phi \cdot \mathbf{c}$, and $\varphi = \Phi^T \mathbf{c}$ into the vector Helmholtz decomposition (SI.2) yields its generalization to second-order tensor fields

$$\mathbf{S} = \nabla \phi + \operatorname{curl} \Phi \quad (\text{SI.8})$$

via (SI.7)₂ and the identity $\nabla(\phi \cdot \mathbf{c}) = (\nabla \phi)^T \mathbf{c}$, again for constant \mathbf{c} . The PeFNO in the paper for divergence-free stress employs the special case

$$\phi = \text{const.} \implies \mathbf{S} = \operatorname{curl} \Phi \quad (\text{SI.9})$$

of (SI.8) analogous to (SI.4).

SI.2.4 Mean-fluctuation split of fields on a region

The PeFNO in the paper is developed for stress fields on a (in general three-dimensional) spatial region U . On such a region, note that any integrable field f can be split into a sum

$$f(\mathbf{x}) = \bar{f} + \tilde{f}(\mathbf{x}), \quad \bar{f} := \frac{1}{v(U)} \int_U f(\mathbf{x}) \, dv(\mathbf{x}), \quad \tilde{f}(\mathbf{x}) := f(\mathbf{x}) - \bar{f}, \quad (\text{SI.10})$$

of mean \bar{f} and fluctuation \tilde{f} parts, where $v(U) = \int_U dv(\mathbf{x})$ is the volume of U . In particular, then, $\mathbf{S} = \bar{\mathbf{S}} + \tilde{\mathbf{S}}$ and $\Phi = \bar{\Phi} + \tilde{\Phi}$ for the tensor fields in (SI.9). Since their mean parts are constant, note that $\operatorname{div} \mathbf{S} = \operatorname{div} \tilde{\mathbf{S}}$ and $\operatorname{curl} \Phi = \operatorname{curl} \tilde{\Phi}$, reducing (SI.9) to

$$\tilde{\mathbf{S}} = \operatorname{curl} \tilde{\Phi} \quad (\text{SI.11})$$

in the context of (SI.10).

SI.3 Application to divergence-free stress

SI.3.1 Stress potential field relations

The potential relation (SI.11) is directly applicable to non-linear quasi-static mechanical equilibrium in solids based on the first PK stress \mathbf{P} , i.e.,

$$\tilde{\mathbf{P}} = \operatorname{curl} \tilde{\mathbf{A}}, \quad (\text{SI.12})$$

where \mathbf{A} is the potential for \mathbf{P} . In contrast to \mathbf{P} , the linear stress tensor \mathbf{T} is symmetric (i.e., $\mathbf{T}^T = \mathbf{T}$), and (SI.11) is not directly applicable. To preserve the symmetry of \mathbf{T} , (SI.11) must be modified by the choice $\tilde{\Phi} = (\operatorname{curl} \tilde{\mathbf{B}})^T$ with \mathbf{B} symmetric. The resulting potential relation

$$\tilde{\mathbf{T}} = \operatorname{inc} \tilde{\mathbf{B}} := \operatorname{curl} (\operatorname{curl} \tilde{\mathbf{B}})^T \quad (\text{SI.13})$$

for \mathbf{T} is then identically symmetric (as evident for example from (SI.17)₃ below) and divergence-free. In linear elasticity, the operator inc is known as the incompatibility operator (e.g., [Teodosiu, 1982](#)), and \mathbf{B} is known as the Beltrami stress potential or "function" (e.g., [Sadd, 2009](#), §13.6).

SI.3.2 Fourier series relations

Assume next that all fields are periodic on U . The Fourier series of any field f integrable and periodic on U is given by

$$f(\mathbf{x}) = \sum_{\mathbf{k} \in U^*} e^{i\mathbf{k} \cdot \mathbf{x}} \hat{f}(\mathbf{k}), \quad \hat{f}(\mathbf{k}) = \frac{1}{v(U)} \int_U e^{-i\mathbf{k} \cdot \mathbf{x}} f(\mathbf{x}) dv(\mathbf{x}), \quad (\text{SI.14})$$

where $i = \sqrt{-1}$ and U^* is the wavevector space of U (examples given below). In particular, then

$$\begin{aligned} \mathbf{P}(\mathbf{x}) &= \sum_{\mathbf{k} \in U^*} e^{i\mathbf{k} \cdot \mathbf{x}} \hat{\mathbf{P}}(\mathbf{k}), & \mathbf{A}(\mathbf{x}) &= \sum_{\mathbf{k} \in U^*} e^{i\mathbf{k} \cdot \mathbf{x}} \hat{\mathbf{A}}(\mathbf{k}), \\ \mathbf{T}(\mathbf{x}) &= \sum_{\mathbf{k} \in U^*} e^{i\mathbf{k} \cdot \mathbf{x}} \hat{\mathbf{T}}(\mathbf{k}), & \mathbf{B}(\mathbf{x}) &= \sum_{\mathbf{k} \in U^*} e^{i\mathbf{k} \cdot \mathbf{x}} \hat{\mathbf{B}}(\mathbf{k}). \end{aligned} \quad (\text{SI.15})$$

The mean-fluctuation split (SI.10) takes the Fourier series form

$$f(\mathbf{x}) = \bar{f} + \tilde{f}(\mathbf{x}), \quad \bar{f} = \hat{f}(\mathbf{0}), \quad \tilde{f}(\mathbf{x}) = \sum_{\mathbf{k} \neq \mathbf{0}} e^{i\mathbf{k} \cdot \mathbf{x}} \hat{f}(\mathbf{k}), \quad (\text{SI.16})$$

with $\sum_{\mathbf{k} \neq \mathbf{0}} := \sum_{\mathbf{k} \in U^* \setminus \{\mathbf{0}\}}$. This implies in particular (recall that \mathbf{B} is symmetric)

$$\begin{aligned} \operatorname{div} \mathbf{P}(\mathbf{x}) &= \operatorname{div} \tilde{\mathbf{P}}(\mathbf{x}) = \sum_{\mathbf{k} \neq \mathbf{0}} e^{i\mathbf{k} \cdot \mathbf{x}} \hat{\mathbf{P}}(\mathbf{k}) i\mathbf{k}, \\ \operatorname{div} \mathbf{T}(\mathbf{x}) &= \operatorname{div} \tilde{\mathbf{T}}(\mathbf{x}) = \sum_{\mathbf{k} \neq \mathbf{0}} e^{i\mathbf{k} \cdot \mathbf{x}} \hat{\mathbf{T}}(\mathbf{k}) i\mathbf{k}, \\ \operatorname{curl} \mathbf{A}(\mathbf{x}) &= \operatorname{curl} \tilde{\mathbf{A}}(\mathbf{x}) = \sum_{\mathbf{k} \neq \mathbf{0}} e^{i\mathbf{k} \cdot \mathbf{x}} \hat{\mathbf{A}}(\mathbf{k}) (\operatorname{axt} i\mathbf{k})^T, \\ \operatorname{inc} \mathbf{B}(\mathbf{x}) &= \operatorname{inc} \tilde{\mathbf{B}}(\mathbf{x}) = \sum_{\mathbf{k} \neq \mathbf{0}} e^{i\mathbf{k} \cdot \mathbf{x}} (\operatorname{axt} i\mathbf{k}) \hat{\mathbf{B}}(\mathbf{k}) (\operatorname{axt} i\mathbf{k})^T. \end{aligned} \quad (\text{SI.17})$$

In the context of the potential relations (SI.12) and (SI.13), then,

$$\begin{aligned} \hat{\mathbf{P}}(\mathbf{k}) &= \begin{cases} \hat{\mathbf{A}}(\mathbf{k}) & \mathbf{k} = \mathbf{0} \\ \hat{\mathbf{A}}(\mathbf{k}) (\operatorname{axt} i\mathbf{k})^T & \mathbf{k} \neq \mathbf{0} \end{cases}, \\ \hat{\mathbf{T}}(\mathbf{k}) &= \begin{cases} \hat{\mathbf{B}}(\mathbf{k}) & \mathbf{k} = \mathbf{0} \\ (\operatorname{axt} i\mathbf{k}) \hat{\mathbf{B}}(\mathbf{k}) (\operatorname{axt} i\mathbf{k})^T & \mathbf{k} \neq \mathbf{0} \end{cases}, \end{aligned} \quad (\text{SI.18})$$

respectively. These also follow from the fact that, since the potential relations involve only the fluctuation parts of the corresponding fields, $\hat{\mathbf{P}}(\mathbf{0}) = \hat{\mathbf{A}}(\mathbf{0})$ and $\hat{\mathbf{T}}(\mathbf{0}) = \hat{\mathbf{B}}(\mathbf{0})$ may be assumed without loss of physical generality.

SI.4 Computational details

SI.4.1 Cartesian component relations

For brevity and simplicity, the treatment in the paper is limited to the non-linear case (SI.12) and Cartesian component relations. In particular,

$$\mathbf{P} = \sum_{i=1}^3 \sum_{j=1}^3 P_{ij} \mathbf{i}_i \otimes \mathbf{i}_j, \quad \mathbf{A} = \sum_{i=1}^3 \sum_{j=1}^3 A_{ij} \mathbf{i}_i \otimes \mathbf{i}_j. \quad (\text{SI.19})$$

These result in the Cartesian component matrix forms

$$\mathbf{P}(\mathbf{x}) = \sum_{\mathbf{k} \in \mathbf{U}^*} e^{i\mathbf{k} \cdot \mathbf{x}} \hat{\mathbf{P}}(\mathbf{k}), \quad \mathbf{A}(\mathbf{x}) = \sum_{\mathbf{k} \in \mathbf{U}^*} e^{i\mathbf{k} \cdot \mathbf{x}} \hat{\mathbf{A}}(\mathbf{k}), \quad (\text{SI.20})$$

of (SI.15)_{1,2}, respectively, with $\mathbf{k} := (k_1, k_2, k_3)$ and $\mathbf{x} := (x_1, x_2, x_3)$. In particular, the output layer in the architecture (light red in Figure 1(a)) of the PgFNO and PiFNO is based on (SI.20)₁. Evaluation of the PiFNO loss function Equation (6) is based on the Cartesian component array form

$$\operatorname{div} \mathbf{P}(\mathbf{x}) = \sum_{\mathbf{k} \neq \mathbf{0}} e^{i\mathbf{k} \cdot \mathbf{x}} \hat{\mathbf{d}}(\mathbf{k}) \quad (\text{SI.21})$$

of (SI.17)₁ with

$$\hat{\mathbf{d}}(\mathbf{k}) := \hat{\mathbf{P}}(\mathbf{k}) i\mathbf{k} = i \begin{bmatrix} \hat{P}_{11}(\mathbf{k}) k_1 + \hat{P}_{12}(\mathbf{k}) k_2 + \hat{P}_{13}(\mathbf{k}) k_3 \\ \hat{P}_{21}(\mathbf{k}) k_1 + \hat{P}_{22}(\mathbf{k}) k_2 + \hat{P}_{23}(\mathbf{k}) k_3 \\ \hat{P}_{31}(\mathbf{k}) k_1 + \hat{P}_{32}(\mathbf{k}) k_2 + \hat{P}_{33}(\mathbf{k}) k_3 \end{bmatrix}. \quad (\text{SI.22})$$

The output transformation $\mathbf{A}^{\text{out}} \rightarrow \mathbf{P}^{\text{out}}$ in the architecture (light red in Figure 1(b)) for the PeFNO is determined by the Cartesian component matrix form

$$\hat{\mathbf{P}}(\mathbf{k}) = \begin{cases} \hat{\mathbf{A}}(\mathbf{k}) & \mathbf{k} = \mathbf{0} \\ \hat{\mathbf{A}}(\mathbf{k}) (\text{axt } i\mathbf{k})^T & \mathbf{k} \neq \mathbf{0} \end{cases}, \quad (\text{SI.23})$$

of (SI.18)₁ with

$$\begin{aligned} & \hat{\mathbf{A}}(\mathbf{k}) (\text{axt } i\mathbf{k})^T \\ &= i \begin{bmatrix} k_2 \hat{A}_{13}(\mathbf{k}) - k_3 \hat{A}_{12}(\mathbf{k}) & k_3 \hat{A}_{11}(\mathbf{k}) - k_1 \hat{A}_{13}(\mathbf{k}) & k_1 \hat{A}_{12}(\mathbf{k}) - k_2 \hat{A}_{11}(\mathbf{k}) \\ k_2 \hat{A}_{23}(\mathbf{k}) - k_3 \hat{A}_{22}(\mathbf{k}) & k_3 \hat{A}_{21}(\mathbf{k}) - k_1 \hat{A}_{23}(\mathbf{k}) & k_1 \hat{A}_{22}(\mathbf{k}) - k_2 \hat{A}_{21}(\mathbf{k}) \\ k_2 \hat{A}_{33}(\mathbf{k}) - k_3 \hat{A}_{32}(\mathbf{k}) & k_3 \hat{A}_{31}(\mathbf{k}) - k_1 \hat{A}_{33}(\mathbf{k}) & k_1 \hat{A}_{32}(\mathbf{k}) - k_2 \hat{A}_{31}(\mathbf{k}) \end{bmatrix} \end{aligned} \quad (\text{SI.24})$$

in the context of (SI.20). On this basis, note for example that

$$\mathbf{P}_{ab}^{\text{out}} = \sum_{\mathbf{k} \in U^*} e^{i\mathbf{k} \cdot \mathbf{x}_b} \hat{\mathbf{P}}_a^{\text{out}}(\mathbf{k}), \quad (\text{div } \mathbf{P}_a^{\text{out}})_b = \sum_{\mathbf{k} \neq 0} e^{i\mathbf{k} \cdot \mathbf{x}_b} \hat{\mathbf{d}}_a^{\text{out}}(\mathbf{k}), \quad (\text{SI.25})$$

hold for $\mathbf{P}_{ab}^{\text{out}}$ and $(\text{div } \mathbf{P}_a^{\text{out}})_b$, respectively, in Equation (5) and Equation (6).

Implementation and numerical evaluation of these relations in the corresponding FNOs is based of course on their truncation and discretization.

SI.4.2 Discrete Fourier transform for real-valued fields

The multi-dimensional discrete Fourier transform (DFT) and its counterpart for real-valued fields (RDFT) represent tensor-product-based direct generalizations of the one-dimensional (1D) case. For this case, let U in (SI.14) represent an interval of length l . Then

$$\begin{aligned} U &= \{\mathbf{x} = x_1 \mathbf{i}_1 \mid x_1 \in [0, l]\}, \\ U^* &= \{\mathbf{k} = k_1 \mathbf{i}_1 \mid k_1 = 2\pi\kappa_1/l, \kappa_1 \text{ integer}\}, \end{aligned} \quad (\text{SI.26})$$

and (SI.14) reduce to

$$f(\xi_1) = \sum_{\kappa_1=-\infty}^{\infty} e^{2\pi i \kappa_1 \xi_1} \hat{f}_{\kappa_1}, \quad \hat{f}_{\kappa_1} = \int_0^1 e^{-2\pi i \kappa_1 \xi_1} f(\xi_1) d\xi_1, \quad (\text{SI.27})$$

with $\xi_1 := x_1/l \in [0, 1]$. Uniform discretization

$$[0, 1] = \bigcup_{i_1=1}^{n_1} [\xi_{i_1}, \xi_{i_1+1}], \quad \xi_{i_1} := (i_1 - 1)/n_1, \quad (\text{SI.28})$$

of $[0, 1]$, trapezoidal integration of (SI.27)₁, order m_1 truncation of (SI.27)₂, and cardinality then determine the discretized form / approximation

$$\begin{aligned} \check{f}_{\kappa_1} &= \frac{1}{n_1} \sum_{i_1=1}^{n_1} \varphi_{\kappa_1 i_1}^- f_{i_1}, \\ f_{i_1} &= \begin{cases} \sum_{\kappa_1=-m_1}^{m_1} \varphi_{\kappa_1 i_1}^+ \check{f}_{\kappa_1} & n_1 \text{ odd, } m_1 = \frac{1}{2}(n_1 - 1) \\ \sum_{\kappa_1=-m_1}^{m_1-1} \varphi_{\kappa_1 i_1}^+ \check{f}_{\kappa_1} & n_1 \text{ even, } m_1 = \frac{1}{2}n_1 \end{cases}, \end{aligned} \quad (\text{SI.29})$$

of (SI.27) with $\varphi_{\kappa_1 i_1}^{\pm} := e^{\pm 2\pi i \kappa_1 (i_1 - 1)/n_1}$, $\hat{f}_{\kappa_1} \approx \check{f}_{\kappa_1}$, and $f_{i_1} := f(\xi_{i_1})$.

If f is real-valued, \hat{f}_{κ_1} in (SI.27) satisfies in addition the symmetry condition

$$\hat{f}_{\kappa_1}^* = \int_0^1 e^{2\pi i \kappa_1 \xi_1} f(\xi_1) d\xi_1 = \hat{f}_{-\kappa_1}, \quad \kappa_1 \neq 0, \quad (\text{SI.30})$$

via the identity $(z_1 z_2)^* = z_1^* z_2^*$, $f^* = f$, and $(e^{-2\pi i \kappa_1 \xi_1})^* = e^{2\pi i \kappa_1 \xi_1}$, where $z^* := x - iy$ is the complex conjugate of $z = x + iy$. This results in the reduced form

$$\begin{aligned} \check{f}_{\kappa_1} &= \frac{1}{n_1} \sum_{i_1=1}^{n_1} \varphi_{\kappa_1 i_1}^- f_{i_1}, \\ f_{i_1} &= \check{f}_0 + \begin{cases} 2 \text{rea} \sum_{\kappa_1=1}^{m_1} \varphi_{\kappa_1 i_1}^+ \check{f}_{\kappa_1} & n_1 \text{ odd, } m_1 = \frac{1}{2}(n_1 - 1) \\ 2 \text{rea} \sum_{\kappa_1=1}^{m_1-1} \varphi_{\kappa_1 i_1}^+ \check{f}_{\kappa_1} + (-1)^{i_1+1} \check{f}_{\frac{1}{2}n_1} & n_1 \text{ even, } m_1 = \frac{1}{2}n_1 \end{cases}, \end{aligned} \quad (\text{SI.31})$$

of (SI.29) with $2 \operatorname{rea} z = z + z^*$, where $x = \operatorname{rea} z$ is the real part of $z = x + iy$. In particular, for n_1 even, (SI.31) is based on modal periodicity $\check{f}_{\kappa_1 \pm n_1} = \check{f}_{\kappa_1}$.

Comparing (SI.29) (f complex-valued) and (SI.31) (f real-valued) for n_1 even, for example, one sees that the former depends on $2m_1$ modes, and the latter on $m_1 + 1$ modes. This reduction in the number of independent modes represents the computational advantage of the RDFT and its fast version (RFFT: e.g., [Sorensen et al., 1987](#)). For the discretization $n_1 = n_{\text{dis}} = 64$ employed in the paper, for example, the corresponding RFFT is based on $\frac{1}{2}n_1 + 1 = 33$ independent modes. Proof-of-concept computations in the paper are carried out for plane deformation in a 2D square region / unit cell U of side length l , i.e.,

$$\begin{aligned} U &= \{\mathbf{x} = x_1 \mathbf{i}_1 + x_2 \mathbf{i}_2 \mid x_d \in [0, l], d = 1, 2\}, \\ U^* &= \{\mathbf{k} = k_1 \mathbf{i}_1 + k_2 \mathbf{i}_2 \mid k_d = 2\pi \kappa_d / l, \kappa_d \text{ integer}, d = 1, 2\}. \end{aligned} \quad (\text{SI.32})$$

Tensor-product-based generalization of (SI.31) to 2D for $n_{1,2}$ even yields

$$\begin{aligned} \check{f}_{\mu_1 \mu_2} &= \frac{1}{n_1 n_2} \sum_{i_1=1}^{n_1} \sum_{i_2=1}^{n_2} \varphi_{\mu_1 i_1}^- \varphi_{\mu_2 i_2}^- f_{i_1 i_2}, & \mu_{1,2} &= 1, \dots, \frac{1}{2}n_{1,2} + 1, \\ \check{f}_{\mu_1 i_2} &= \check{f}_{\mu_1 1} + 2 \operatorname{rea} \sum_{\mu_2=2}^{\frac{1}{2}n_2} \varphi_{\mu_2 i_2}^+ \check{f}_{\mu_1 \mu_2} + (-1)^{i_2+1} \check{f}_{\mu_1 \frac{1}{2}n_2+1}, & i_2 &= 1, \dots, n_2, \\ f_{i_1 i_2} &= \check{f}_{1 i_2} + 2 \operatorname{rea} \sum_{\mu_1=2}^{\frac{1}{2}n_1} \varphi_{\mu_1 i_1}^+ \check{f}_{\mu_1 i_2} + (-1)^{i_1+1} \check{f}_{\frac{1}{2}n_1+1 i_2}, & i_1 &= 1, \dots, n_1, \end{aligned} \quad (\text{SI.33})$$

for f real-valued via modal periodicity and re-indexing $\mu_d = \kappa_d + 1$, with now

$$\varphi_{\mu_d i_d}^\pm := e^{\pm 2\pi i (\mu_d - 1)(i_d - 1)/n_d}. \quad (\text{SI.34})$$

Actual calculations employ of course the fast version of (SI.33).

SI.4.3 The case of plane deformation

Restricting attention to (x_1, x_2) -plane deformation as in the paper,

$$\mathbf{F} = \begin{bmatrix} F_{11} & F_{12} & 0 \\ F_{21} & F_{22} & 0 \\ 0 & 0 & 1 \end{bmatrix}, \quad \mathbf{E} = \begin{bmatrix} E_{11} & E_{12} & 0 \\ E_{12} & E_{22} & 0 \\ 0 & 0 & 0 \end{bmatrix}, \quad \mathbf{P} = \begin{bmatrix} P_{11} & P_{12} & 0 \\ P_{21} & P_{22} & 0 \\ 0 & 0 & P_{33} \end{bmatrix}, \quad (\text{SI.35})$$

hold for the deformation gradient, symmetric Green strain, and first PK stress, respectively. In particular, the form of \mathbf{E} follows from that of \mathbf{F} via Equation (4), and the form of \mathbf{P} from both of these in the context of the isotropic elastic Saint Venant-Kirchhoff relation Equation (3). Likewise, the reduced form

$$\mathbf{A} = \bar{\mathbf{A}} + \tilde{\mathbf{A}}, \quad \bar{\mathbf{A}} = \begin{bmatrix} \bar{A}_{11} & \bar{A}_{12} & 0 \\ \bar{A}_{21} & \bar{A}_{22} & 0 \\ 0 & 0 & \bar{A}_{33} \end{bmatrix}, \quad \tilde{\mathbf{A}} = \begin{bmatrix} 0 & 0 & \tilde{A}_{13} \\ 0 & 0 & \tilde{A}_{23} \\ \tilde{A}_{31} & \tilde{A}_{32} & 0 \end{bmatrix}, \quad (\text{SI.36})$$

of \mathbf{A} applies in this case, consistent with (SI.35)₃. In this context, the fast version of (SI.33) is applied to each non-zero component of $\mathbf{P}_{i_1 i_2}$ and $\check{\mathbf{P}}_{\mu_1 \mu_2}$ in each hidden layer of the Pg- and PiFNO architectures in Figure 1(a). In the latter case, $\check{\mathbf{P}}_{\mu_1 \mu_2}^{\text{out}}$ determine

$$\begin{aligned}\check{\mathbf{d}}_{\mu_1 \mu_2}^{\text{out}} &= \frac{2\pi\imath}{l} \check{\mathbf{P}}_{\mu_1 \mu_2}^{\text{out}} (\mu_1 - 1, \mu_2 - 1, 0) \\ &= \frac{2\pi\imath}{l} \begin{bmatrix} (\mu_1 - 1) \check{P}_{11 \mu_1 \mu_2}^{\text{out}} + (\mu_2 - 1) \check{P}_{12 \mu_1 \mu_2}^{\text{out}} \\ (\mu_1 - 1) \check{P}_{21 \mu_1 \mu_2}^{\text{out}} + (\mu_2 - 1) \check{P}_{22 \mu_1 \mu_2}^{\text{out}} \\ 0 \end{bmatrix}, \quad (\mu_1, \mu_2) \neq (1, 1),\end{aligned}\quad (\text{SI.37})$$

in the context of discretized, truncated form of (SI.21) for evaluation of $\text{div } \mathbf{P}_a^{\text{out}}$ in the PiFNO loss function Equation (6). Analogously, the fast version of (SI.33) is applied to each non-zero component of $\mathbf{A}_{i_1 i_2}$ and $\check{\mathbf{A}}_{\mu_1 \mu_2}$ in each hidden layer of the PeFNO architecture. Lastly, the discretized form of (SI.23), i.e.,

$$\check{\mathbf{P}}_{\mu_1 \mu_2}^{\text{out}} = \begin{cases} \check{\mathbf{A}}_{11}^{\text{out}} & (\mu_1, \mu_2) = (1, 1) \\ \frac{2\pi\imath}{l} \check{\mathbf{A}}_{\mu_1 \mu_2}^{\text{out}} [\text{axt}(\mu_1 - 1, \mu_2 - 1, 0)]^T & (\mu_1, \mu_2) \neq (1, 1) \end{cases} \quad (\text{SI.38})$$

with

$$\begin{aligned}\check{\mathbf{A}}_{\mu_1 \mu_2}^{\text{out}} [\text{axt}(\mu_1 - 1, \mu_2 - 1, 0)]^T \\ = \begin{bmatrix} (\mu_2 - 1) \check{A}_{13 \mu_1 \mu_2}^{\text{out}} - (\mu_1 - 1) \check{A}_{13 \mu_1 \mu_2}^{\text{out}} & 0 \\ (\mu_2 - 1) \check{A}_{23 \mu_1 \mu_2}^{\text{out}} - (\mu_1 - 1) \check{A}_{23 \mu_1 \mu_2}^{\text{out}} & 0 \\ 0 & (\mu_1 - 1) \check{A}_{32 \mu_1 \mu_2}^{\text{out}} - (\mu_2 - 1) \check{A}_{31 \mu_1 \mu_2}^{\text{out}} \end{bmatrix},\end{aligned}\quad (\text{SI.39})$$

determines the transformation $\mathbf{A}^{\text{out}} \rightarrow \mathbf{P}^{\text{out}}$ in the output layer of Figure 1(b) for the PeFNO, again via component-wise application of (SI.33) in its fast version.